Particle fracture regimes from impact simulations

Duc Chung Vu,[1,2,*] Lhassan Amarsid,[1,†] Jean-Yves Delenne,[3,‡] Vincent Richefeu,[4,§] and Farhang Radjai[2,‖]
[1]*CEA, DES, IRESNE, DEC, SESC, LDOP, Saint Paul les Durance 13108, France*
[2]*LMGC, CNRS, University of Montpellier, Montpellier 34090, France*
[3]*IATE, INRAE, Institut Agro, University of Montpellier, Montpellier 34000, France*
[4]*3SR, CNRS, University of Grenoble Alpes, Grenoble 38400, France*

(Received 12 February 2024; accepted 9 April 2024; published 29 April 2024)

We introduce an approach to particle breakage, wherein the particle is modeled as an aggregate of polyhedral cells with their common surfaces governed by the Griffith criterion of fracture. This model is implemented within a discrete element code to simulate and analyze the breakage behavior of a single particle impacting a rigid plane. We find that fracture dynamics involves three distinct regimes as a function of the normalized impact energy ω. At low values of ω, the particle undergoes elastic rebound and no cracks occur inside the particle. In the intermediate range, the particle is damaged by nucleation and propagation of cracks, and the effective restitution coefficient declines without breakup of the particle. Finally, for values of ω beyond a well-defined threshold, the particle breaks into fragments and the restitution coefficient increases with ω due to kinetic energy carried away by the fragments. We show that particle damage, restitution coefficient, and fracture efficiency (the amount of energy input consumed for particle fracture) collapse well as a function of dimensionless scaling parameters. Our data are also sufficiently accurate to scale fragment size and shape distributions. It is found that fragment masses (volumes) follow a power-law distribution with an exponent decreasing with fracture energy. Interestingly, the average elongation and flatness of fragments are very close to those observed in experiments and lunar samples at the optimal fracture efficiency.

DOI: 10.1103/PhysRevE.109.044907

I. INTRODUCTION

Particle breakage is a commonly observed phenomenon in natural flows and industrial processes involving powders and grains [1–5]. Particle breakage is usually undesirable, but it also represents the goal of milling operations, which are known for their energy intensive nature. Despite extensive past research, particle breakage mechanisms in granular materials remain poorly understood due to their multiscale nature, involving material subparticle scales to particle scales, and up to the packing and process scales [6–9]. The fragmentation of particles is controlled by the mechanical properties of the particles and their contacts, on one hand, and the process operational factors, on the other hand [10–15]. For instance, the distribution of fragment sizes during the grinding process in ball mills is influenced by the cohesive strength of single particles, numbers and sizes of grinding balls, amount of granular material, and other system parameters [14,15]. The particles can break under various loading modes such as compression, distortion, shear, and impact. Different fracture modes generally take place simultaneously during a comminution process in different parts of the system [16]. To model particle breakage, an important issue is therefore to identify physical mechanisms at different scales: subparticle processes at the origin, the strength and potential weaknesses of particles, single-particle fracture by impact or forces exerted by other particles, collective dynamics of particles, and process-scale mechanisms of energy supply to the particles.

Experimental studies of single-particle fragmentation have been carried out to analyze the fragment mass and size distributions, crack patterns, and failure modes. The masses in the range of small fragments are often found to follow a power-law distribution with exponents that do not always seem to be universal, but depend on the brittle or ductile nature of fracture and dimensionality of the object [9,17–23]. A general observation is that during impact between two particles, plastic deformation develops first around the contact point, then cracks appear and propagate through the particle, and eventually split the particle [17,24]. A part of the supplied energy is consumed in producing new fracture surfaces inside the particle, while a large amount of the supplied energy is also taken away in the form of the kinetic energy of the fragments after collision and dissipated by plastic deformations and frictional or inelastic collisions. Impact-induced fragmentation was found experimentally to generate elongated shapes characterized by the dimensions a, b, and c of their bounding box. In several reported investigations, the ratios were found to be distributed around the proportions $a : b : c \simeq 2 : \sqrt{2} : 1$ [25–28].

Due to the inherent complexity of the experimental measurement of dynamic fracture of a single particle or the

*duc-chung.vu@cea.fr
†lhassan.amarsid@cea.fr
‡jean-yves.delenne@umontpellier.fr
§vincent.richefeu@3sr-grenoble.fr
‖franck.radjai@umontpellier.fr

evolution of a collection of particles in real time, particle dynamics simulations based on the discrete element method (DEM) have also been developed as an alternative approach for the investigation of particle breakage in granular materials. For example, experimental findings of fragment size distributions were reproduced by such simulations [29–32]. Important results were obtained by DEM simulations, such as crossover from a damaged state to the fragmented state at a well-defined value of impact energy [10,27,33–35]. The critical point of this transition was identified as the impact velocity for which the average fragment mass takes a maximum value [35,36]. The effects of material properties such as interface energy on the fracture pattern were also investigated [37,38].

A DEM-based model extensively used for particle fragmentation is known as the bonded particle method (BPM) that simulates a parent particle as an aggregate of spherical particles [12,32,38,39]. For primary spheres, since the external boundary of the aggregate is used to represent the particle surface and the aggregate is porous, the volume is not conserved during fragmentation. In contrast, the primary polyhedra can fill the volume of a particle with zero porosity and no volume is lost during particle breakage [36,40–42]. Furthermore, in a cluster of polyhedra, the bonds coincide with the common surfaces between polyhedra, so that the breakage of a bond naturally creates a fracture surface. Particle tessellation into contiguous polyhedra was coined the bonded cell method (BCM) [40]. In BCM, each face-face interaction represents a potential crack and the fracture energy is obtained by multiplying the area by surface energy [40,42]. The cell-meshed particles, when they are randomly distributed, allow for arbitrary fragment shapes if the number of primary polyhedra composing the particle is sufficiently high [40].

Particle fracture by BCM requires a fracture criterion. Numerical studies reported in the literature are generally based on force or stress thresholds which lead to brittle behavior, while fracture mechanics requires a model fully based on energy [12,27,32,36,40,41]. In their model of a thermodynamically consistent breakup model, Orozco *et al.* [42] used a criterion based on the fracture energy in the framework of the contact dynamics method (nonsmooth DEM), which does not account for elastic deflections at the contact points [43]. For this reason, the debonding criterion was based on the amount of energy absorbed by an interface and it was postulated that an interface between two adjacent cells breaks if the total amount of energy exceeds the fracture energy. Using this criterion, they were able to scale particle breakage as a function of the impact energy in three-dimensional (3D) single-particle impact and the evolution of grinding in ball mills [14,42].

In this paper, we use BCM with a fracture law that is based on the Griffith criterion of crack propagation by accounting for elastic energy release in each interface. In other words, the initial formulation of this criterion in terms of the incremental creation of a new fracture area is coarse grained for application to finite surface creation. Thus a cell-cell interface breaks only if the total elastic energy stored per unit interface area exceeds two times the specific fracture energy. We investigate in detail the breakage of a single particle impacting a rigid plane by means of extensive simulations. We analyze particle damage, fracture efficiency, and restitution coefficient as a function of impact energy. We propose functional forms that capture well the behavior in each fracture regime and transition between different regimes and we compare our data with those of Orozco *et al.* [42]. We also have enough data to analyze the resulting fragment size distributions and particle shapes. As we shall see, our findings are consistent with previous studies, but they provide a more general picture in the range of weak impact velocities where rebound and damage of the particle occur without particle fragmentation.

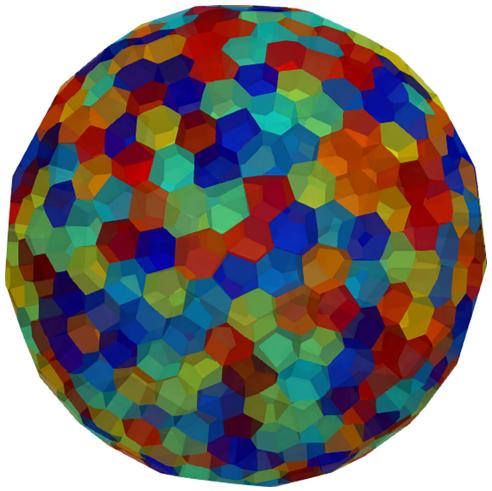

FIG. 1. Particle model generated by Voronoi tessellation with 1728 polyhedral cells represented by different colors.

In the following, we first introduce, in Sec. II, the fracture model, boundary conditions, and parameters of impact simulations. The fracture regimes are analyzed in terms of particle damage, fracture efficiency, and effective restitution coefficient in Sec. III as a function of impact parameters. In Sec. IV, we show that the fracture variables and regimes scale with the ratio of impact energy to cohesion energy. In Sec. V, we analyze the distributions of fragment shapes and sizes. Finally, we discuss the most salient results of this work in Sec. VI.

II. BONDED CELL METHOD AND RUPTURE MODEL

A. Voronoi tessellation

We use the bonded cell method (BCM) based on the division of the particle into polyhedral cells interacting with their neighboring cells via an interface characterized by a fracture energy. Each particle is divided into 1728 cells by Voronoi tessellation using the NEPER software [44]. One possible technique to construct the centroidal Voronoi tessellation is known as the Lloyd's method, which simply alternates between constructing Voronoi tessellations and mass centroids [41,45,46]. An example of the particle model composed of polyhedral cells is shown in Fig. 1. For the sake of geometrical consistency between the shape of the parent particle and its constitutive polyhedral cells, we use a *truncated pentakis dodecahedron* shape composed of 92 faces involving 12 regular pentagons, 20 regular hexagons, and 60 mirror-symmetric hexagons. The cells (primary particles) have random sizes and shapes, but they are always convex and share their faces with

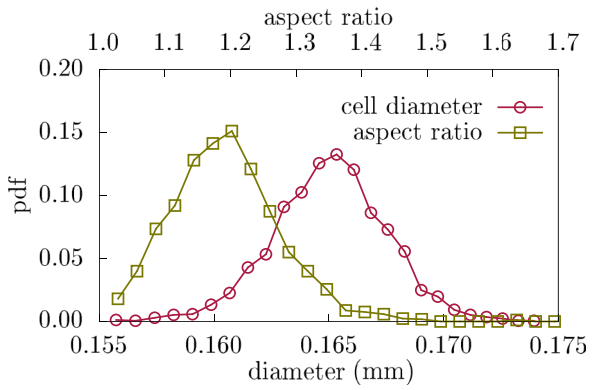

FIG. 2. Distributions of the aspect ratios and sizes of primary particles.

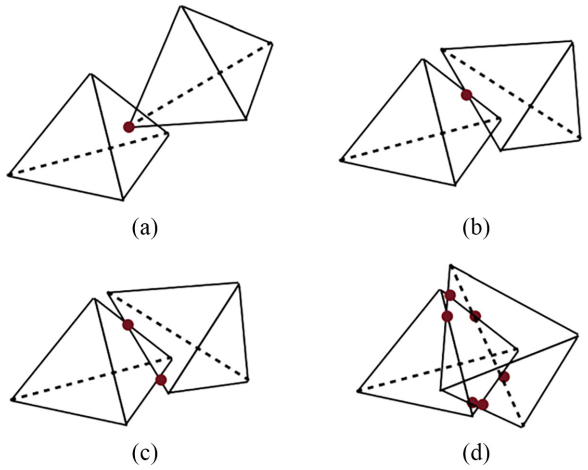

FIG. 3. Different types of contacts between two polyhedra: (a),(b) simple contact, (c) double (edge-face) contact, and (d) triple (face-face) contact.

their neighboring cells. A key numerical parameter of BCM is the number of cells in the particles (both the parent particle and its progeny) to ensure arbitrary fragment shapes and a meaningful range of fragment sizes. For instance, several phenomena such as particle shattering, surface breakage, and damage without breakage are well captured by the simulation, but the number of cells must be sufficiently high to avoid fragment shapes after shattering that are controlled by initial Voronoi tessellation [14,40]. It has also been observed that the fracture process is influenced by the number of cells if it is below 100 [14,41].

Figure 2 displays the size and shape distribution of the primary particles generated by Voronoi tessellation. The aspect ratio of a cell is defined as the ratio of the longest dimension to the shortest dimension of its bounding box. The diameter of a cell is defined as the diameter of a sphere having the same volume as the polyhedral cell. We see that the aspect ratios of cells range between 1 and 1.3, with a mean value around 1.2. Cell diameters mostly range from 0.16 to 0.17 mm, so that the cell sizes are approximately equal. The sizes of the parent particle and cells are the upper and lower bounds, respectively, of the size distribution of fragments in the debris generated by particle fracture. The statistical representativity of the distribution of fragment sizes in the process of fragmentation depends therefore on their ratio. It is also noteworthy that BCM makes it possible to account for subparticle defects (pores, precracks, etc.) and other inhomogeneities (cell size gradients, cell shapes, etc.) by means of biased tessellation of the particle. In our simulations, the particle is assumed to be homogeneous and defectless, with the goal of concentrating on the fracture regimes.

B. Interactions between polyhedra

In our simulation model, primary polyhedral cells are smoothed by means of a Minkowski sum with a sphere of desired radius (Minkowski radius). As a consequence, each polyhedron consists of three subelements, namely, the vertex which is a small sphere, the edge which is a cylinder connecting two vertices, and the face which is a plane connecting at least three vertices. The contacts between two polyhedra are represented by the contacts of its subelements, leading to six contact types, such as vertex-face, edge-edge, vertex-edge, vertex-vertex, edge-face, and face-face interactions. The unilateral constraints associated with these contact types do not have the same dimension. The vertex-face, vertex-edge, vertex-vertex, and edge-edge interactions involve a single contact point, which can be handled in the same way as contacts between spherical particles. Such simple contacts represent a single unilateral constraint; see Figs. 3(a) and 3(b). In contrast, a face-face contact is a plane that needs at least three points for its definition. Therefore, a face-face contact is equivalent to three simple contacts or unilateral constraints [43,47,48]. This implies that at least three contact points are necessary to represent a face-face contact between two rigid polyhedra. Note that the number of contact points can be larger than 3 depending on the number of edges, but the number of independent constraints is always 3; see Fig. 3(d). In a similar vein, full representation of an edge-face interaction needs at least two contact points; see Fig. 3(c). Thus the edge-face and face-face contacts can be described as "double" and "triple" contacts, respectively.

The Voronoi tessellation of the parent particle leads to a configuration of polyhedral cells that have face-face, vertex-vertex, and parallel edge-edge contacts. We consider only the face-face contacts to define cohesive interfaces. The edge-edge and vertex-vertex contacts in the cell configurations are assumed to carry no surface energy and are neglected since the internal cohesion of the particle is carried by the interfaces. However, as the interfaces break and the generated fragments move during particle fracture, other contact types may appear and they will be treated as frictional cohesionless contacts due to the irreversible nature of fracture.

At each contact point between cells, either a linear or a nonlinear force law can be implemented. For smooth particle surfaces with well-defined curvatures at the contact point, the Hertz law can be used. However, in this paper, due to the faceted shapes of the cells, we use the linear elastic law which is equivalent to a linear spring acting on the contact point. This means that the behavior of the particle as a whole is linear elastic. Note also that since the cells are treated as rigid bodies, the particle volume changes are only due to the

overlaps between cells and the particle has a linear elastic behavior as a whole.

Let $\vec{n}$ and $\vec{t}$ be the normal and tangential unit vectors at a contact point c between particles i and j. The force $\vec{f} = f_n\vec{n} + f_t\vec{t}$ acting by particle j on particle i at this point of the interface is expressed as a function of the normal relative displacement (overlap) δ_n and cumulative tangential displacement $\vec{\delta}_t$. The normal force law is expressed as [49,50]

$$f_n = -k_n\delta_n - 2\alpha\sqrt{k_n m}\,\dot{\delta}_n, \tag{1}$$

where k_n is the normal stiffness of intercell bonds, δ_n is the normal displacement (with the sign convention that $\delta_n < 0$ is an overlap and $\delta_n > 0$ is a gap), $\dot{\delta}_n$ is the relative normal velocity, m is the reduced mass of the two particles, and the dimensionless damping number α takes a value between 0 and 1. The viscous damping term accounts for normal energy dissipation and α is a function of the normal restitution coefficient e_n [51–54],

$$\alpha = \begin{cases} \frac{-\log e_n}{\sqrt{(\log e_n)^2+\pi^2}} & \text{for } 0 < e_n \leqslant 1 \\ 1 & \text{for } e_n = 0. \end{cases} \tag{2}$$

It is useful to remember here that the use of viscous damping does not mean that the real source of dissipation is the viscous behavior of the particles. In DEM, the normal restitution coefficient is a convenient physical parameter that accounts for contact inelasticity. However, the method used to impose its value between 0 and 1 is not essential as long as it does not produce artifacts depending on the context. The tangential force is given by [43,55,56]

$$\vec{f}_t = -k_t\vec{\delta}_t - 2\alpha\sqrt{k_n m}\,\vec{v}_t, \tag{3}$$

where k_t is the tangential stiffness, and $\vec{v}_t = \dot{\vec{\delta}}_t$ is the relative tangential velocity. For internal bonds between cells, there is no friction unless the interface fails and transforms into a frictional contact; see below. Hence, as long as an interface between two cells has not failed, the only source of dissipation is viscous damping.

C. Rupture criterion

Thermodynamically, the creation of cohesionless surface and crack propagation obeys the Griffith criterion. According to this criterion, a crack propagates if the rate of elastic potential energy released by surface creation is above the fracture energy. The Griffith formulation is based on a differential criterion with the assumption that crack growth is a continuous process. Hence, it cannot be applied as such to a cell-cell interface of finite area $\mathcal{S}$ in BCM. For this reason, a "coarse-grained" form of the energy criterion should be applied by considering a finite variation ΔW_p of the elastic energy. This condition for the creation of a surface equal to $\mathcal{S}$ can be expressed as [14,57]

$$-\frac{\Delta W_p}{2\mathcal{S}} = G \geqslant G_c, \tag{4}$$

where G_c is fracture energy per unit surface, the so-called toughness, and G is the energy release rate.

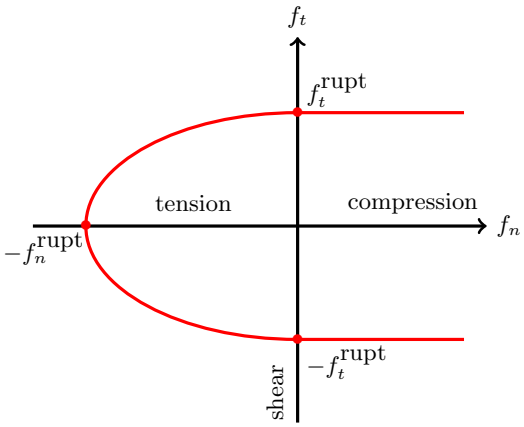

FIG. 4. Strength envelope of a single contact point belonging to an interface between polyhedral primary cells.

Since the elastic energy associated with the interface vanishes when the bond fails, ΔW_p is actually the total potential elastic energy of the interface. Furthermore, since the compressive failure threshold is very high compared to the threshold in tension, we set the threshold in compression to infinity. Hence, ΔW_p must involve only the forces in tension,

$$\Delta W_p = \sum_{i\in\mathcal{S}} \left[\frac{f_{ni}^2}{2k_n} H(\delta_{ni}) + \frac{f_{ti}^2}{2k_t} \right], \tag{5}$$

where $H(\delta_{ni})$ is the Heaviside function defined by

$$H(\delta_{ni}) = \begin{cases} 0 & \text{if } \delta_{ni} \leqslant 0 \\ 1 & \text{if } \delta_{ni} > 0. \end{cases} \tag{6}$$

This assumption implies that compressive forces do not contribute to fracture. Figure 4 shows a strength envelope based on Eqs. (4) and (5). This envelope is simplified by considering a single contact point belonging to the interface. Since the interface involves at least three contact points, the strength envelope should be represented in a six-dimensional space.

Once $G \geqslant G_c$, the cohesive bond fails and all contacts of this interface become frictional without cohesion. If the gap created as a result of interface deformation is nonzero ($\delta_n > 0$), the normal and tangential forces are both zero and the newly created contact is open. Otherwise ($\delta_n \leqslant 0$), the contact remains active and the relation between the normal force f_n and the overlap δ_n is given by Eq. (1). Note that when the viscous damping term makes f_n negative, we set f_n to zero. This is necessary to avoid negative normal forces at cohesionless contacts [58]. In our simulations, we also set the restitution coefficient e_n for frictional contacts to a value close to zero, while the restitution coefficient for internal bonds between cells is high; see Table I.

The tangential force at frictional contacts is governed by the Coulomb friction law,

$$f_t = \min\{|k_t\vec{\delta}_t|,\ \mu_s f_n\}, \tag{7}$$

where k_t is tangential stiffness of the frictional contact, and μ_s is the interparticle friction coefficient. The orientation of the tangential force $\vec{t}$ is opposite to either the relative elastic displacement $\vec{\delta}_t$ below the Coulomb threshold or the relative

TABLE I. Simulation parameters for impact test of a particle with a rigid plane.

Parameter	Symbol	Value	Unit
No. cells	N_c	1728	
Particle density	ρ_s	6000	kg/m^3
Gravity acceleration	g	0	m/s^2
Impact velocity	v_0	[0.5;10]	m/s
For frictional contacts:			
Normal stiffness	k_n	10^8	N/m
Tangential stiffness	k_t	8×10^7	N/m
Restitution coefficient	e_n^2	0.001	
Friction coefficient	μ_s	0.3	
For cohesive bonds between cells:			
Normal stiffness	k_n	10^7	N/m
Tangential stiffness	k_t	0.8×10^7	N/m
Restitution coefficient	e_n^2	0.999	
Fracture energy	G_c	[0.2;2.0]	J/m^2

velocity $\vec{v}_t$ at the contact point when the Coulomb threshold is reached.

D. Impact parameters

We performed 3D impact tests of a single particle with a rigid plane. The particle is placed close to the horizontal plane and given an initial velocity v_0. The impact energy (kinetic energy before collision) is varied by changing the impact velocity in the range given in Table I. This wide variation of v_0 allows us to investigate particle fracture as a function of impact energy varying over at least two orders of magnitude. The parent particle diameter is 2 mm in all tests. Each impact test was repeated five times, each with a different and independent tessellation of the particle into cells. All the data points presented in this paper correspond therefore to average values over the five tests, with an error bar representing their standard deviation. We note that the point of impact with the plane should be random to allow the particle to fall on a face, edge, or vertex. To avoid systematic errors due to this effect, we rotated the particle in a random direction with a random angle before each impact test. As we shall see below, the error bars are generally small, meaning that particle orientation has little effect on the fragmentation process.

For the parametric study of fracture regimes, we also changed the value of the fracture energy G_c from 0.2 to 2 Jm^{-2}. This range is broad enough to allow us to analyze its effect on fracture regimes and the scaling of the fracture data in combination with impact energy. All other system parameters were kept constant and their values are shown in Table I. The parameters are different for cohesive bonds between cells, which encode the internal mechanical behavior of the particles, and for frictional contacts between fragments. In particular, the restitution coefficient e_n is set to a value (0.999) close to 1 between cells in order to minimize internal dissipation due to inelasticity, in contrast to previous simulations in which e_n between cells was set to zero. It would have been possible to set $e_n = 1$, but we kept the possibility of a small amount of internal dissipation in order to see whether it can have a significant effect on the behavior. As we shall see, this is not the case. In contrast, the restitution coefficient between fragments and between the fragments and the bottom wall was set to a value (0.001) very close to zero in order to better identify the source of the overall restitution coefficient e_k of the particle due to the transfer of kinetic energy to the fragments when the particle breaks. The effect of the restitution coefficient at the impact point between the particle and the bottom walls on the fracture behavior requires an independent investigation.

The friction coefficient μ_s was set to 0.3 between fragments. This is a typical value of friction coefficient in most materials. The friction coefficient between cells before fracture is not defined since cell-cell interfaces are governed by elastic interactions. We do not expect μ_s to play a significant role in impact tests since we consider a head-on impact and the generated fragments after impact follow mainly diverging trajectories. The gravity g is zero. As a result, the kinetic energy of the particle is fully determined by its initial velocity. The initial kinetic energy also depends on the particle density ρ, which was set to 6000 kg m^{-3} to mimic high-density metal oxides, although its effect on impact tests is physically expressed through the impact energy. The normal stiffness k_n was set to a high enough value to avoid large overlaps between fragments and between the particle and rigid plane. The largest overlap occurs for the highest impact energy. We therefore set k_n for frictional contacts to 10^8 Nm^{-1}, which leads to an overlap $\simeq 0.0025d$ with the rigid plane, where $d = 2$ mm is the diameter of the particle. Since the cells inside the particles receive much lower kinetic energies due to energy dissipation and their large number inside the particle, we set k_n between cells to a value 10 times lower. The tangential stiffness was set to $k_t = 0.8k_n$ for the interface between cells and for frictional contacts, corresponding to the Poisson ratio $\nu = 1/3$, which is a typical value for many materials [59]. Note that the effect of k_n on fracture is through the expression of energy release rate G in Eqs. (4) and (5).

III. PARTICLE FRACTURE REGIMES

During an impact, part of the initial kinetic energy $W_k^- = mv^2/2$ of the particle is transmitted to the fragments. Note that v is the precollision velocity of the particle. Since the particle is placed very close to the rigid plane, we have $v \simeq v_0$. Let W_k^+ be the total kinetic energy of the fragments after collision. The difference, $W_d = W_k^- - W_k^+$, is consumed in fracture and other dissipative interactions, including friction and inelastic collisions between fragments and with the rigid plane. If $\mathcal{A}$ is the total cohesionless surface area created during fracture, the total fracture energy is given by

$$W_f = 2\mathcal{A}G_c. \tag{8}$$

We also define the total surface energy $W_s = 2\mathcal{A}_0 G_c$, which is the total energy required to break all interfaces of the total initial area $\mathcal{A}_0$. Hence, particle damage D_w can be defined as

$$D_w = \frac{W_f}{W_s} = \frac{\mathcal{A}}{\mathcal{A}_0}. \tag{9}$$

By definition, D_w varies from 0 to 1.

Figure 5 displays particle damage D_w as a function of impact velocity v, for different values of fracture energy G_c.

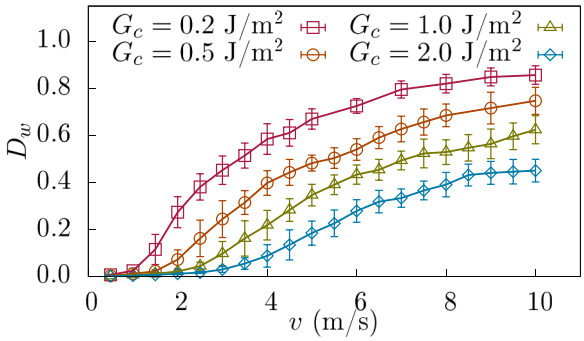

FIG. 5. Particle damage D_w vs impact velocity v for different values of fracture energy G_c. For each test, the error bar represents standard deviation over five independent tests.

The damage first increases rapidly with v and then slowly tends to a constant value. The maximum value of damage is below 1, meaning that despite huge initial kinetic energy, the cell-cell interfaces do not break entirely apart. As we shall see, since the number of primary cells is sufficiently high, elongated fragments composed of several cell-cell interfaces are generated. Examples of particle fragmentation are shown in Fig. 6 for several values of fracture energy G_c with impact velocity $v = 4.5$ m/s. Obviously, the damage of a particle with smaller values of G_c is higher at the same impact velocity v and increases faster than those of larger G_c. We also see that the error bars are small, indicating that the variability of fracture as a result of the variations of impact position is not significant.

In the comminution process, the amount of energy consumed for fracture as a function of impact energy is an important aspect that must be thoroughly considered. We define fracture efficiency η as the ratio of the total energy W_f consumed for fracture to the impact energy,

$$\eta = \frac{W_f}{W_k^-}. \tag{10}$$

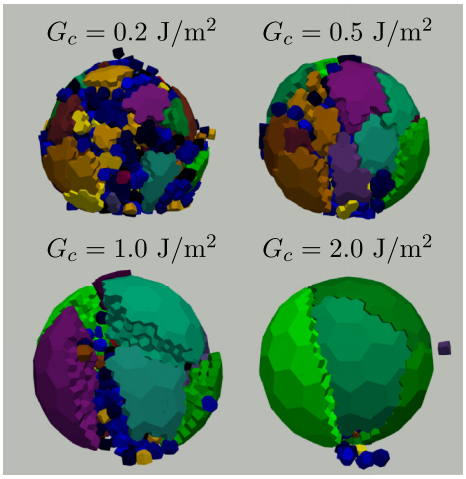

FIG. 6. Fragmentation of a particle impacting a rigid wall for different values of fracture energy G_c. The simulation was carried out with an impact velocity of 4.5 m/s.

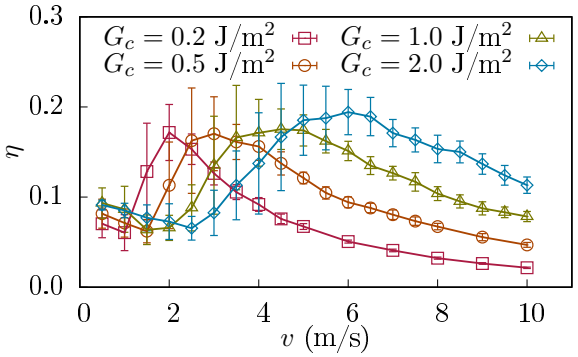

FIG. 7. Fracture efficiency η vs impact velocity v for different values of fracture energy G_c.

Comminution is generally not an efficient process in the sense that most of the supplied energy is not consumed in fracture. It is thus interesting to see how the value of η for a single particle depends on the impact parameters.

The evolution of η as a function of impact velocity v for different values of G_c is shown in Fig. 7. We see that fracture efficiency first decreases to a minimum value of the order of 0.05 and then increases rapidly with v up to a peak value of the order of 0.2. After the peak, it slowly declines towards a nonzero asymptotic value depending on G_c. The velocity at which η takes its peak value increases with G_c. The variation of η in our study is consistent with previous studies [42], except for the initial decrease of η at low impact velocity v. This decrease as a function of impact velocity reflects energy loss by inelastic interactions and the opening of cracks inside the particle in the vicinity of the impact point. Since cracked interfaces are governed by frictional contact interactions, the loss of energy at the increasing number of such contacts grows with velocity and leads to a lower amount of energy available for fracture. Note, also, that the velocity at which η reaches its minimum value increases with G_c. The nonmonotonic behavior of the evolution of η means that there is a characteristic velocity at which the conversion of the kinetic energy to fracture is optimal. As we shall see, below and above the characteristic velocity, the supplied energy is essentially either dissipated by inelastic collisions or taken away by the fragments.

During fragmentation, the kinetic energy of the parent particle can be dissipated by viscous damping between the particle and the rigid plane, plastic deformation, and damage of the particle or transferred to the generated fragments. We define an effective restitution coefficient e_k from the ratio of the pre-impact and post-impact kinetic energies,

$$e_k^2 = \frac{W_k^+}{W_k^-}. \tag{11}$$

The evolution of e_k^2 as a function of impact velocity is shown in Fig. 8. Consistently with the initial decrease of η, the squared restitution coefficient e_k^2 decreases from a value close to 1 since the restitution coefficient between primary cells is close to 1. From a value of v at which fracture efficiency η reaches its minimum, e_k^2 starts rapidly declining to a minimal value that decreases with increasing fracture energy G_c, and

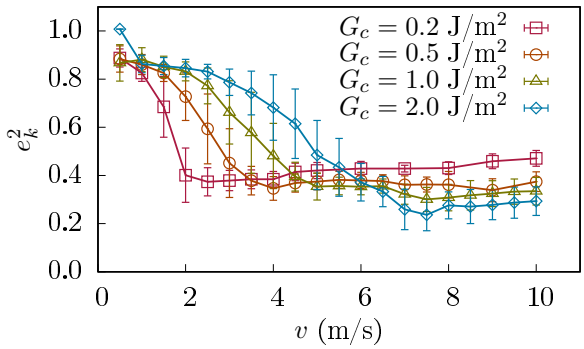

FIG. 8. Squared restitution coefficient e_k^2 as a function of impact velocity v for different values of fracture energy G_c.

then increases again. The restitution coefficient at high impact velocity is larger for lower values of G_c.

IV. SCALING BEHAVIOR

The results presented so far show that the evolutions of fracture variables D_w, η, and e_k^2 as a function of v differ according to the value of the fracture energy G_c. This is an expected behavior since the amount of fracture created by impact energy W_k^- is directly dependent on the surface energy. We define a normalized impact energy ω by the ratio of supplied energy W_k^- to the total interface energy W_s of the particle,

$$\omega = \frac{W_k^-}{W_s}. \tag{12}$$

We naturally expect that the simulation data collapse when expressed as a function of ω. Following Ref. [60], we refer to ω as *damage potential*.

Figure 9 displays the evolution of e_k^2 as a function of ω on the log-log scale. We see that all data points fall into three distinct regimes with two well-defined crossover values ω_0 and ω_1. The data nearly collapse on a master curve in the first two regimes, but differ slightly in the third regime. In the range $\omega < \omega_0 \simeq 0.3$, e_k^2 decreases slowly with ω. In this regime, the particle is not broken and only a small fraction of

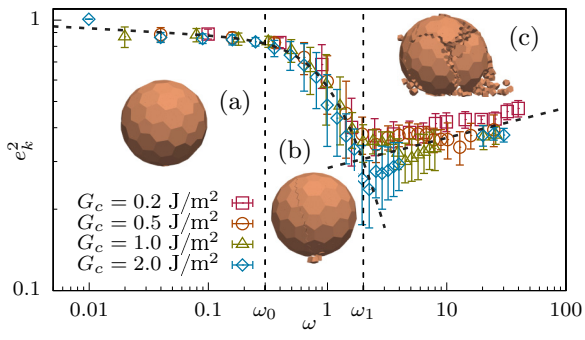

FIG. 9. Squared restitution coefficient e_k^2 as a function of normalized impact energy ω on a log-log scale for different values of fracture energy G_c. The dotted lines are the fitting forms of Eqs. (13) and (14). The vertical dashed lines mark transition points between different regimes.

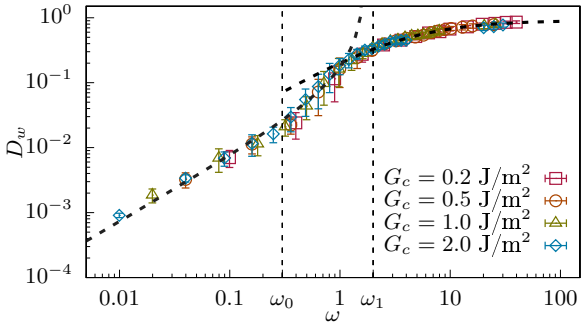

FIG. 10. Particle damage D_w as a function of the normalized impact energy ω on a log-log scale. The dotted lines are the fitting forms shown in Eqs. (15) and (16). The vertical dashed lines indicate transition points between different regimes.

the supplied energy is used to create cracks at the impact point. The decrease of e_k^2 can be attributed to the fact that the normal restitution coefficient between the particle and the rigid plane is close to zero and the restitution coefficient between cells is not strictly equal to 1. It is, however, remarkable that e_k is above 0.9 in this range.

In the range of intermediate values, $\omega_0 < \omega < \omega_1 \simeq 2.0$, the restitution coefficient declines rapidly with increasing ω due to the creation of an increasing number of cracks inside the particle. Finally, in the range $\omega_1 < \omega$, the particle breaks into an increasing number of fragments and the restitution coefficient increases slowly with ω. It is noteworthy that the first two regimes of Fig. 9 were not observed in the simulations of Ref. [42] due to the low value of the restitution coefficient in those simulations. But the crossover to particle fragmentation occurs at the same value $\omega_1 \simeq 2.0$ as in our simulations, despite differences in the numerical methods that are employed.

Figure 9 also shows that the whole range of the first two regimes $\omega < \omega_1$ is well fit to a double power-law function,

$$e_k^2 = \frac{1}{a\left(\frac{\omega}{\omega_0}\right)^m + b\left(\frac{\omega}{\omega_0}\right)^n}, \tag{13}$$

with prefactors $a = 0.058$ and $b = 1.165$, and exponents $m = 1.9$ and $n = 0.024$. The data do not exactly collapse as a function of ω in the second and third regimes. Higher values of G_c lead to lower values of e_k at ω_1. The values of the parameters for the above fitting form slightly depend on G_c. We used the highest value of G_c to obtain their values. It is also remarkable that in the third regime, the data seem to tend to an asymptotic power-law function as ω increases,

$$e_k^2 = c\left(\frac{\omega}{\omega_1}\right)^k, \tag{14}$$

where $c = 0.3$ and $k = 0.11$.

Figure 10 shows particle damage D_w as a function of ω. Here, all the data nicely collapse on a single increasing function of ω. In the low-energy regime, D_w increases from 10^{-3} to 10^{-2}. In the second regime, it increases faster, from 10^{-2} to 0.2. In the third regime, it increases from 0.2 towards 1. For the first two regimes, the following fitting function captures

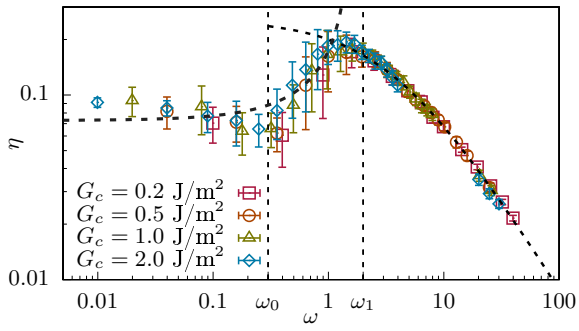

FIG. 11. Fracture efficiency η as a function of normalized impact energy ω. The dotted lines are the fitting forms (17) and (18). The vertical dashed lines indicate transition points between different regimes.

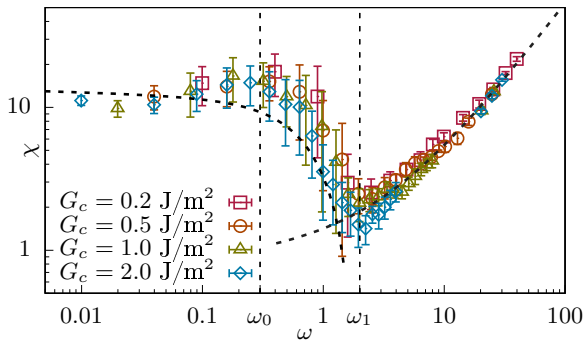

FIG. 12. Fragmentation efficiency η as a function of the normalized impact energy ω. The dotted lines are the fitting forms (21) and (22). The vertical dashed lines indicate transition points between different regimes.

the data well:

$$D_w = \frac{a'(\omega/\omega_0)}{1 + b'(\omega/\omega_0)}, \tag{15}$$

with $a' = 0.022$ and $b' = -0.175$. In the high-energy regime, the following form is well suited to the data:

$$D_w = \frac{c'(\omega/\omega_1)}{1 + d'(\omega/\omega_1)}, \tag{16}$$

where $c' = d' = 0.403$, ensuring that as $\omega \to \infty$, D_w tends to 1.

According to Eqs (9) and (10), we have $\eta = D_w/\omega$. We may therefore express η as a function of ω from that of D_w. Hence, for the low- and intermediate-energy regimes, we have

$$\eta = \frac{a'/\omega_0}{1 + b'(\omega/\omega_0)}. \tag{17}$$

For the high-energy regime, we have

$$\eta = \frac{c'/\omega_1}{1 + d'(\omega/\omega_1)}. \tag{18}$$

The evolution of fracture efficiency η as a function of ω together with these fitting forms are displayed in Fig. 11. In the first regime, η decreases slightly from 0.1. However, in the second regime where part of the supplied energy contributes to crack nucleation, η increases with ω before reaching the peak value around $\omega = \omega_1$. We see that the fitting form (17) does not exactly capture the initial decrease of η, but it follows the data points within the available statistical precision. The third regime is excellently captured by the proposed fit. In this regime, η declines although particle damage D_w increases. This means that the amount of energy contributing to particle breakage increases, but it requires an excess energy supply which increases faster, thereby leading to a fast reduction of η.

It is important to note that the choice of the numerical values of ω_0 and ω_1 was based on the observation of the generation of cracks and particle fragmentation. Indeed, for $\omega > \omega_0$, cracks begin to form inside the particle, and for $\omega > \omega_1$, the particle breaks into at least two fragments. These transition points have nearly the same value for the five independent tests performed for each set of parameters. We also have seen that they are consistent with the evolution of restitution coefficient, fracture efficiency, and damage as a function of damage potential ω.

Another variable of interest is the ratio χ of the post-impact kinetic energy to the fracture energy,

$$\chi = \frac{W_k^+}{W_f}. \tag{19}$$

This variable quantifies the relative weight of the energy transported by the fragments with respect to that consumed in particle breakage. It can be expressed as a function of e_k and η,

$$\chi = \frac{e_k^2}{\eta}. \tag{20}$$

Given the fitting forms of e_k and η as a function of ω, the evolution of χ in the first and second regimes must be captured by the following fitting form:

$$\chi = \frac{\omega_0 + b'\omega}{a'a\left(\frac{\omega}{\omega_0}\right)^m + a'b\left(\frac{\omega}{\omega_0}\right)^n}, \tag{21}$$

and for the third regime by

$$\chi = \frac{c}{c'}(\omega_1 + d'\omega)\left(\frac{\omega}{\omega_1}\right)^k. \tag{22}$$

The evolution of χ as a function of ω on the log-log scale is shown in Fig. 12 for different values of G_c. The fitting form is close to the data points in the first two regimes within statistical precision, but does not capture the trend in the first regime well, while in the third regime, it follows the data points well. The value of χ increases from 10 to 18 in the first regime, implying that the kinetic energy of fragments is high compared to the energy consumed for fracture, which should be vanishingly small in the absence of crack generation. Then, it decreases in the second regime at which the energy consumed for crack generation increases faster than kinetic energy. It reaches its minimum value coinciding with the peak of η, as shown in Fig. 11. At this point, we have $\chi \simeq 1$, which means that the amount of energy consumed at this point for fracture is nearly equal to that carried away by the fragments. In the third regime, χ increases again due to the faster increase of the kinetic energy of fragments than the energy consumed by breakage.

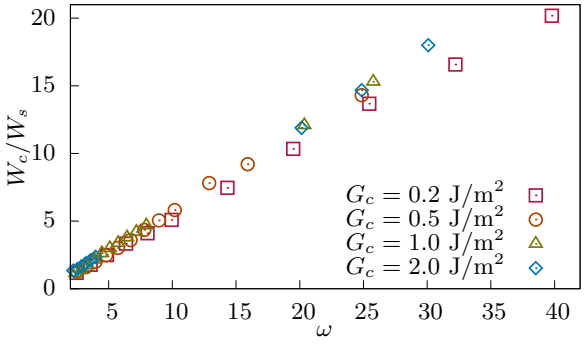

FIG. 13. Normalized energy dissipated by inelastic collisions and friction W_c/W_s vs normalized impact energy ω for $\omega > \omega_1$.

It is also interesting to consider the energy W_c dissipated by inelastic collisions and friction,

$$W_c = W_k^- - W_k^+ - W_f. \tag{23}$$

We normalize this energy by the total surface energy W_s and the following expression can be easily established:

$$\frac{W_c}{W_s} = \omega\left(1 - \eta - e_k^2\right). \tag{24}$$

The evolution of this ratio as a function of ω is displayed in Fig. 13 for $\omega > \omega_1$, where particle breakage occurs. It increases almost linearly with ω with slope $\simeq 1/2$ up to very high values of ω. This implies that approximately half of the supplied kinetic energy is dissipated by contact inelasticity and friction when the particle breaks. The remaining half is either used for fracture or carried away by the fragments.

V. FRAGMENT SIZES AND SHAPES

The shapes and sizes of the fragments reflect the fragmentation process. Several experimental studies have shown that the fragments of rock generated by explosion or impact have an elongated shape and the probability distribution of the fragment masses is a power-law function [9,25,26,32]. To define an appropriate shape descriptor, we construct the bounding box of each fragment with principal axis $c \leqslant b \leqslant a$, as shown in Fig. 14. The length a of the bounding box is the longest dimension of the fragment, b is the largest distance perpendicular to the direction of a, and c is defined as the

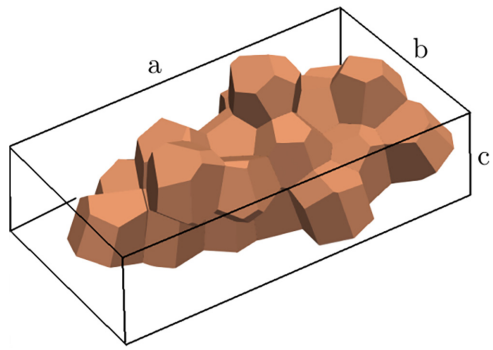

FIG. 14. The space dimensions of a fragment according to its bounding box in three mutually orthogonal planes ($a \geqslant b \geqslant c$).

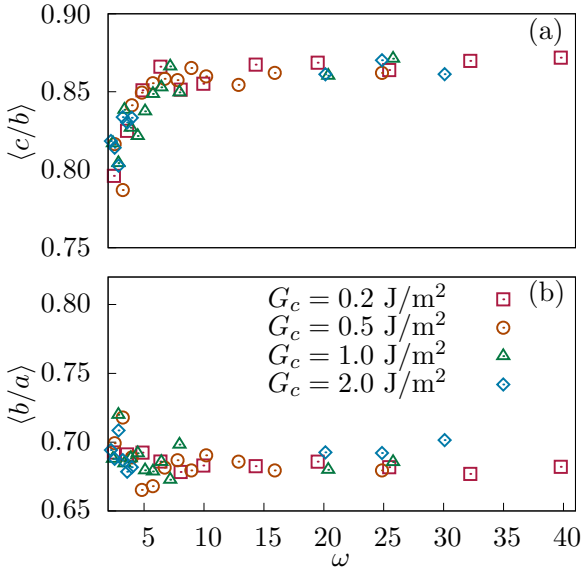

FIG. 15. The average shape descriptors as a function of normalized impact energy ω for all values of fracture energy G_c, with (a) the flatness ratio $\langle c/b \rangle$ and (b) the elongation ratio $\langle b/a \rangle$.

largest distance perpendicular to the plane determined by a and b. The shapes of the fragments can be described in terms of the elongation ratio b/a and flatness ratio c/b. The inverse values a/b and b/c represent the two aspect ratios.

We consider the average value of the elongation ratio and flatness ratio calculated over all fragments generated as a result of particle breakage. We neglect the fragments composed of a single primary cell in order to remove the effect of Voronoi tessellation. The values of $\langle c/b \rangle$ and $\langle b/a \rangle$ are shown in Fig. 15 as a function of ω for $\omega > \omega_1$. The minimum values of elongation ratio $\langle b/a \rangle$ and flatness ratio $\langle c/b \rangle$ are $\simeq 0.69$ and $\simeq 0.77$, respectively. The ratio c/b increases and tends to a constant value $\simeq 0.88$, while b/a slightly decreases and remains constant and equal to 0.69.

Interestingly, these values are comparable to the data obtained from particle size and shape distributions in lunar samples [25,26,61]. Since only limited amounts of lunar soil were retrieved during the Apollo missions, the particle shapes were studied using micro-x-ray computed tomography of simulant granular materials manufactured based on real lunar samples [26]. Disregarding very fine particles, the distributions of the grain shapes were found to have an average flatness ratio 0.694 ± 0.143 and an average elongation ratio 0.723 ± 0.132, which are quite close to their values of the fragments in our simulations. It has been argued that this ratio represents a *self-similar shape*: once broken into two equal fragments, each fragment has the same elongation ratio as the parent particle [26]. Mathematically, the ratio of self-similar shape by this operation is $\sqrt{2}/2 \simeq 0.7$. In our simulations, the particle does not break in successive steps, but the average value of the elongation ratio suggests that a self-similar crack propagation process occurs inside the particle during its breakage.

Another quantity that has been used for the characterization of particle shape is the shape factor S_f defined as [9]

$$S_f = (1/a + 1/b + 1/c)\sqrt{a^2 + b^2 + c^2}/\sqrt{3}. \tag{25}$$

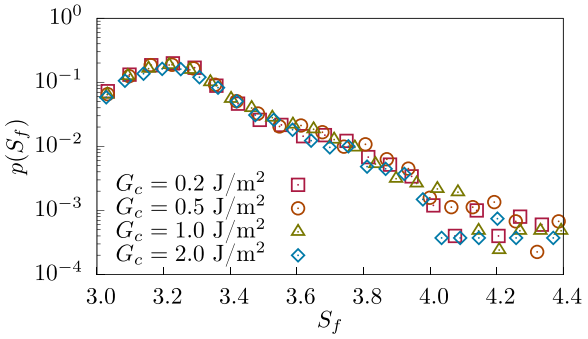

FIG. 16. Probability distribution of the shape factor S_f on a semilogarithmic plot for all values of fracture energy G_c and impact velocity v.

This parameter reaches its lowest value $S_f = 3$ for nearly spherical fragments with $a \simeq b \simeq c$, while elongated shapes have larger values, $S_f > 3$. To quantify the statistics of occurrence of different shapes of fragments, we determined the probability distribution $p(S_f)$ of the shape factor. Note that we gather data of fragment shapes for different impact velocities v together to gain large enough data sets to calculate the distribution function. Figure 16 shows that the simulation data for all values of G_c collapse on a curve which has a decreasing exponential form for $S_f > 3.2$. This is in remarkable agreement with the experimental results of Ref. [9], although the fragments in our simulations result from single-particle fracture rather than a multiparticle granular process. The mean value of S_f is about 3.3 for all cases in our simulations.

We also investigated the probability distribution $p(m)$ of fragment masses. Several previous studies suggest that the distribution is generically a power-law function,

$$p(m) \sim m^{-\tau}. \tag{26}$$

It seems that the value of the exponent τ is not universal, but depends on the material or the amount of energy consumed for fragmentation [7,9,29,62–64]. Figure 17 presents the fragment mass distributions $p(m)$ for different values of fracture energy G_c on the log-log scale. The masses of fragments m are normalized by the maximum mass $m_{\max}$. We observe here a power-law behavior for all values of G_c. The value of the exponent at $G_c = 0.2$ J/m^2 is $\tau = 3.0$, but decreases as G_c increases. For $G_c = 2.0$ J/m^2, we find $\tau = 2.1$. The value of τ in our study is higher than the value $\tau = 5/3$ proposed for three-dimensional solids [9,29,32,65]. It is important to recall here again that particle size distribution resulting from the comminution of a granular material is a consequence of the combined effects of stress distribution inside the material and single-particle fragmentation process. For this reason, the size and shape distributions of single-particle impact may differ from those of a granular process involving multicontact stress transmission.

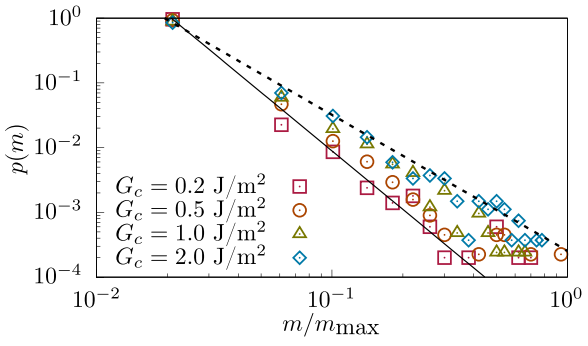

FIG. 17. Fragment mass distributions $p(m)$ for different values of the fracture energy G_c. The solid line shows the power function (26) with $\tau = 3.0$ for $G_c = 0.2$ J/m^2 and the dotted line with $\tau = 2.1$ for $G_c = 2.0$ J/m^2.

VI. CONCLUSIONS

In this paper, a fracture law based on the Griffith criterion was used with the bonded cell method implemented in a 3D DEM code for the simulation of the fracture behavior of a single particle impacting a rigid plane. The particle is discretized by means of Voronoi tessellation into polyhedral cells whose interfaces represent potential cracks while the cells and their combinations represent potential fragments. The fracture law implies that a cell-cell interface fails if the energy release rate is above the fracture energy. Our results of single-particle fracture compare well with both past simulations of the same process and recent experimental data.

Our simulations show that the behavior of the impacting particle involves three distinct regimes depending on the *damage potential* ω, defined as the ratio of impact energy to the fracture energy of the particle. Our results are consistent with previous experimental and numerical findings, in which our first two regimes correspond to a damaged state and the high-energy regime is coincident with the fragmented state. This behavior makes two critical values of the damage potential appear, which determine whether the particle breaks or simply rebounds with or without being damaged. For different values of fracture energy, we showed that several physical variables such as particle damage, restitution coefficient, fracture efficiency, and the amount of energy dissipated by inelastic collisions and friction are well scaled by ω. The fracture efficiency is a nonmonotonic function of impact energy with its optimal value at the crossover to the third regime, where particles break into several pieces. We found that in the third regime, nearly half of the input energy is dissipated by contact inelasticity and friction, the other half being either consumed for fracture or carried away by the fragments generated as a result of particle breakage.

We also found that the distribution of fragment masses is a power-law function with an exponent slightly decreasing with fracture energy. It is remarkable that the shape descriptors of the fragments such as flatness ratio and elongation ratio have generic values previously observed in real samples of granular materials. In particular, we found that the fragments in the whole range of values of ω have an average aspect ratio which is nearly equal to $\sqrt{2}$, a value that hints at a self-similar shape. This self-similarity is consistent with the existence of a power-law size distribution, which is a consequence of the absence of characteristic lengths (between cell size and initial particle size) in the system.

It will be important to extend this work to a broader parametric study to assess the generality of the scaling behavior

evidenced in this work. For example, the initial particle used in our simulations is undamaged and its total surface energy W_s is constant. It will be interesting to consider damaged particles (containing precracks) to study the effect of varying W_s on the dependence of the restitution coefficient and damage on ω. Furthermore, the restitution coefficient between cells can be set to lower values to study its effect on the two first regimes and the crossover values of ω. In the same way, it is important to consider the effect of the restitution coefficient at the impact point between the particle and the bottom walls on the effective restitution e_k coefficient of the particle.

Longer term, we would like to use our results to predict the fracture of particles in rotating drums and during quasistatic deformation of granular materials. Extensive simulations will be performed in both configurations for the scaling of particle breakage as a function of system parameters to obtain clues for the scale-up of comminution from the particle scale to a collection of particles.

ACKNOWLEDGMENTS

The authors acknowledge financial support by SIFCO project (CEA), EDF, and ORANO.

All authors equally contributed to the methodology, data curation, formal analysis, investigation, software, visualization, and writing.

There are no conflicts of interest.

[1] N. L. Johnson, P. H. Krisko, J.-C. Liou, and P. D. Anz-Meador, NASA's new breakup model of EVOLVE 4.0, Adv. Space Res. **28**, 1377 (2001).

[2] S. Michaux and N. Djordjevic, Influence of explosive energy on the strength of the rock fragments and SAG mill throughput, Mineral. Eng. **18**, 439 (2005).

[3] P. J. Hajduk and J. Greer, A decade of fragment-based drug design: Strategic advances and lessons learned, Nat. Rev. Drug Discov. **6**, 211 (2007).

[4] P. Galvez and H. Ivan, Analysis of the state of the art of blast-induced fragment conditioning, Mineral. Eng. **24**, 1638 (2011).

[5] J. A. Sanchidrián, F. Ouchterlony, P. Segarra, and P. Moser, Size distribution functions for rock fragments, Intl. J. Rock Mech. Mining Sci. **71**, 381 (2014).

[6] D. Touil, S. Belaadi, and C. Frances, Energy efficiency of cement finish grinding in a dry batch ball mill, Cement Concrete Res. **36**, 416 (2006).

[7] J. A. Aström, Statistical models of brittle fragmentation, Adv. Phys. **55**, 247 (2006).

[8] I. Bailon-Poujol, J.-P. Bailon, and G. L'Espérance, Ball-mill grinding kinetics of master alloys for steel powder metallurgy applications, Powder Technol. **210**, 267 (2011).

[9] G. Domokos, F. Kun, A. A. Sipos, and T. Szabó, Universality of fragment shapes, Sci. Rep. **5**, 9147 (2015).

[10] H. A. Carmona, F. K. Wittel, F. Kun, and H. J. Herrmann, Fragmentation processes in impact of spheres, Phys. Rev. E **77**, 051302 (2008).

[11] C. Hosten and H. Cimilli, The effects of feed size distribution on confined-bed comminution of quartz and calcite in piston-die press, Intl. J. Miner. Process. **91**, 81 (2009).

[12] F. K. Wittel, Single particle fragmentation in ultrasound assisted impact comminution, Granul. Matter **12**, 447 (2010).

[13] L. Liu, K. D. Kafui, and C. Thornton, Impact breakage of spherical, cuboidal and cylindrical agglomerates, Powder Technol. **199**, 189 (2010).

[14] L. F. Orozco, J.-Y. Delenne, P. Sornay, and F. Radjai, Scaling behavior of particle breakage in granular flows inside rotating drums, Phys. Rev. E **101**, 052904 (2020).

[15] L. F. Orozco, D.-H. Nguyen, J.-Y. Delenne, P. Sornay, and F. Radjai, Discrete-element simulations of comminution in rotating drums: Effects of grinding media, Powder Technol. **362**, 157 (2020).

[16] I. Govender, Granular flows in rotating drums: A rheological perspective, Mineral. Eng. **92**, 168 (2016).

[17] R. Majzoub and M. M. Chaudhri, High-speed photography of low-velocity impact cracking of solid spheres, Philos. Mag. Lett. **80**, 387 (2000).

[18] Y. S. Cheong, A. D. Salman, and M. J. Hounslow, Effect of impact angle and velocity on the fragment size distribution of glass spheres, Powder Technol. **138**, 189 (2003).

[19] H. Katsuragi, D. Sugino, and H. Honjo, Scaling of impact fragmentation near the critical point, Phys. Rev. E **68**, 046105 (2003).

[20] H. Katsuragi, D. Sugino, and H. Honjo, Crossover of weighted mean fragment mass scaling in two-dimensional brittle fragmentation, Phys. Rev. E **70**, 065103(R) (2004).

[21] M. Khanal, W. Schubert, and J. Tomas, Ball impact and crack propagation - Simulations of particle compound material, Granul. Matter **5**, 177 (2004).

[22] W. Schubert, M. Khanal, and J. Tomas, Impact crushing of particle-particle compounds–Experiment and simulation, Intl. J. Miner. Process. **75**, 41 (2005).

[23] S. Z. Wu, K. T. Chau, and T. X. Yu, Crushing and fragmentation of brittle spheres under double impact test, Particle Break. **143-144**, 41 (2004).

[24] J. Tomas, M. Schreier, T. Gröger, and S. Ehlers, Impact crushing of concrete for liberation and recycling, Powder Technol. **105**, 39 (1999).

[25] T. Michikami, A. Hagermann, T. Kadokawa, A. Yoshida, A. Shimada, S. Hasegawa, and A. Tsuchiyama, Fragment shapes in impact experiments ranging from cratering to catastrophic disruption, Icarus **264**, 316 (2016).

[26] M. Takashi, K. Jun, U. Kentaro, T. Akira, and N. Tsukaka, 3D shape characterization and image-based DEM simulation of the lunar soil simulant FJS-1, J. Aerospace Eng. **22**, 15 (2009).

[27] G. Ma, W. Zhou, Y. Zhang, Q. Wang, and X. Chang, Fractal behavior and shape characteristics of fragments produced by the impact of quasi-brittle spheres, Powder Technol. **325**, 498 (2018).

[28] G. Buscarnera and I. Einav, The mechanics of brittle granular materials with coevolving grain size and shape, Proc. R. Soc. A: Math. Phys. Eng. Sci. **477**, 20201005 (2021).

[29] F. Wittel, F. Kun, H. J. Herrmann, and B. H. Kröplin, Fragmentation of shells, Phys. Rev. Lett. **93**, 035504 (2004).

[30] J. A. Åström, F. Ouchterlony, R. P. Linna, and J. Timonen, Universal dynamic fragmentation in d dimensions, Phys. Rev. Lett. **92**, 245506 (2004).

[31] F. Kun, F. K. Wittel, H. J. Herrmann, B. H. Kröplin, and K. J. Måløy, Scaling behavior of fragment shapes, Phys. Rev. Lett. **96**, 025504 (2006).

[32] G. Timár, J. Blömer, F. Kun, and H. J. Herrmann, New universality class for the fragmentation of plastic materials, Phys. Rev. Lett. **104**, 095502 (2010).

[33] C. Thornton, K. K. Yin, and M. J. Adams, Numerical simulation of the impact fracture and fragmentation of agglomerates, J. Phys. D **29**, 424 (1996).

[34] B. Behera, F. Kun, S. McNamara, and H. J. Herrmann, Fragmentation of a circular disc by impact on a frictionless plate, J. Phys.: Condens. Matter **17**, S2439 (2005).

[35] G. Timár, F. Kun, H. A. Carmona, and H. J. Herrmann, Scaling laws for impact fragmentation of spherical solids, Phys. Rev. E **86**, 016113 (2012).

[36] H. A. Carmona, A. V. Guimarães, J. S. Andrade, I. Nikolakopoulos, F. K. Wittel, and H. J. Herrmann, Fragmentation processes in two-phase materials, Phys. Rev. E **91**, 012402 (2015).

[37] K. D. Kafui and C. Thornton, Numerical simulations of impact breakage of a spherical crystalline agglomerate, Powder Technol. **109**, 113 (2000).

[38] R. Moreno-Atanasio and M. Ghadiri, Mechanistic analysis and computer simulation of impact breakage of agglomerates: Effect of surface energy, Chem. Eng. Sci. **61**, 2476 (2006).

[39] B. K. Mishra and C. Thornton, Impact breakage of particle agglomerates, Intl. J. Miner. Process. **61**, 225 (2001).

[40] D.-H. Nguyen, É. Azéma, P. Sornay, and F. Radjaï, Rheology of granular materials composed of crushable particles, Europhys. J. E **41**, 50 (2018).

[41] D. Cantor, E. Azéma, P. Sornay, and F. Radjai, Three-dimensional bonded-cell model for grain fragmentation, Comput. Particle Mech. **4**, 441 (2017).

[42] L. F. Orozco, J.-Y. Delenne, P. Sornay, and F. Radjai, Discrete-element model for dynamic fracture of a single particle, Intl. J. Solids Struct. **166**, 47 (2019).

[43] F. Radjai and V. Richefeu, Contact dynamics as a nonsmooth discrete element method, Adv. Dynam. Granul. Mater. **41**, 715 (2009).

[44] R. Quey, P. R. Dawson, and F. Barbe, Large-scale 3D random polycrystals for the finite element method: Generation, meshing and remeshing, Comput. Methods Appl. Mech. Eng. **200**, 1729 (2011).

[45] Q. Du, M. Emelianenko, and L. Ju, Convergence of the Lloyd algorithm for computing centroidal Voronoi tessellations, SIAM J. Numer. Anal. **44**, 102 (2006).

[46] C. Fang, Z. Nie, J. Gong, B. Li, W. Hu, and A. Mohammed, Discrete element simulation of effects of multicontact loading on single particle crushing, Particuology **69**, 49 (2022).

[47] E. Azéma, F. Radjai, and F. Dubois, Packings of irregular polyhedral particles: Strength, structure, and effects of angularity, Phys. Rev. E **87**, 062203 (2013).

[48] D. C. Vu, L. Amarsid, J.-Y. Delenne, V. Richefeu, and F. Radjai, Macro-elasticity of granular materials composed of polyhedral particles, Granul. Matter **26**, 6 (2024).

[49] J. J. Moreau, Sorne numerical methods in multibody dynamics: Application to granular materials, Europ. J. Mech. A: Solids **13**, 93 (1994).

[50] F. Radjai and F. Dubois, *Discrete-element Modeling of Granular Materials* (Wiley-Iste, New York, 2011).

[51] M. Y. Louge, Computer simulations of rapid granular flows of spheres interacting with a flat, frictional boundary, Phys. Fluids **6**, 2253 (1994).

[52] N. V. Brilliantov, F. Spahn, J.-M. Hertzsch, and T. Pöschel, Model for collisions in granular gases, Phys. Rev. E **53**, 5382 (1996).

[53] K. A. Ismail and W. J. Stronge, Impact of viscoplastic bodies: Dissipation and restitution, J. Appl. Mech. **75**, 061011 (2008).

[54] P. Müller, D. Krengel, and T. Pöschel, Negative coefficient of normal restitution, Phys. Rev. E **85**, 041306 (2012).

[55] M. Jean, The nonsmooth contact dynamics method, Comput. Methods Appl. Mech. Eng. **177**, 235 (1999).

[56] C. Thornton, S. J. Cummins, and P. W. Cleary, An investigation of the comparative behaviour of alternative contact force models during inelastic collisions, Powder Technol. **233**, 30 (2013).

[57] D. Leguillon, Strength or toughness? A criterion for crack onset at a notch, Europ. J. Mech. A: Solids **21**, 61 (2002).

[58] T. Schwager and T. Pöschel, Coefficient of restitution and linear-dashpot model revisited, Granul. Matter **9**, 465 (2007).

[59] I. Agnolin and J.-N. Roux, Internal states of model isotropic granular packings. I. Assembling process, geometry, and contact networks, Phys. Rev. E **76**, 061302 (2007).

[60] L. E. Laczák and G. Károlyi, On the impact of a rigid–plastic missile into rigid or elastic target, Intl. J. Nonlinear Mech. **91**, 1 (2017).

[61] L. M. Le Pen, W. Powrie, A. Zervos, S. Ahmed, and S. Aingaran, Dependence of shape on particle size for a crushed rock railway ballast, Granul. Matter **15**, 849 (2013).

[62] F. Kun and H. J. Herrmann, Transition from damage to fragmentation in collision of solids, Phys. Rev. E **59**, 2623 (1999).

[63] H. Katsuragi, S. Ihara, and H. Honjo, Explosive fragmentation of a thin ceramic tube using pulsed power, Phys. Rev. Lett. **95**, 095503 (2005).

[64] P. Kekäläinen, J. A. Åström, and J. Timonen, Solution for the fragment-size distribution in a crack-branching model of fragmentation, Phys. Rev. E **76**, 026112 (2007).

[65] A. Bershadskii, Some classification of fragmentation processes related to fracture, J. Phys. A: Math. Gen. **33**, 2179 (2000).